

# Gemini GMOS–IFU spectroscopy of the compact H II galaxies Tol 0104-388 and Tol 2146-391: The dependence on the properties of the interstellar medium

P. Lagos<sup>1\*</sup>, E. Telles<sup>2</sup>, A. Nigoche-Netro<sup>3</sup> and E. R. Carrasco<sup>4</sup>

<sup>1</sup>*Centro de Astrofísica da Universidade do Porto, Rua das Estrelas, 4150-762 Porto, Portugal*

<sup>2</sup>*Observatório Nacional, Rua José Cristino, 77, Rio de Janeiro, 20921-400, Brazil*

<sup>3</sup>*Instituto de Astronomía y Meteorología, Av. Vallarta 2602. Col. Arcos Vallarta. Guadalajara, Jalisco. C.P. 44130 México.*

<sup>4</sup>*Gemini Observatory/AURA, Southern Operations Center, Casilla 603, La Serena, Chile*

23 June 2018

## ABSTRACT

Using GMOS–IFU spectroscopic observations of the compact H II/BCD galaxies Tol 0104-388 and Tol 2146-391, we study the spatial distribution of emission lines, equivalent width  $EW(H\beta)$ , extinction  $c(H\beta)$ , ionization ratios ( $[OIII] \lambda 5007/H\beta$ ,  $[SII] \lambda\lambda 6717, 6731/H\alpha$  and  $[NII] \lambda 6584/H\alpha$ ), kinematics, and the chemical pattern (O/H, N/H and N/O) of the warm interstellar medium in these galaxies. We also investigate a possible dependence of these properties on the  $I(He II \lambda 4686)/I(H\beta)$  ratio and find no significant correlation between these variables. In fact, the oxygen abundances appear to be uniform in the regions where the He II  $\lambda 4686$  emission line was measured. It can be interpreted in the sense that these correlations are related to global properties of the galaxies and not with small patches of the interstellar medium. Although a possible weak N/H gradient is observed in Tol 2146-391, the available data suggest that the metals from previous star-formation events are well mixed and homogeneously distributed through the optical extent of these galaxies. The spatial constancy of the N/O ratio might be attributed to efficient transport and mixing of metals by starburst-driven super-shells, powered by a plethora of unresolved star cluster in the inner part of the galaxies. This scenario agrees with the idea that most of the observed He II  $\lambda 4686$  emission line, in our sample of galaxies, is produced by radiative shocks.

**Key words:** galaxies: dwarf – galaxies: individual: Tol 0104-388 – galaxies: individual: Tol 2146-391 – galaxies: ISM – galaxies: abundances.

## 1 INTRODUCTION

The ionizing radiation from newly formed stars and its interaction with the surrounding gas generate collisionally excited and recombination emission lines, that are commonly observed in starburst and low metallicity ( $1/50Z_{\odot}$ – $1/3Z_{\odot}$ ; Kunth & Sargent 1983) dwarf galaxies, such as, H II or blue compact dwarf (BCD) galaxies. From recent studies it was concluded that the hardness of the ionizing radiation from the current star formation (SF) activity increases with decreasing metallicity (e.g., Guseva et al. 2000; Schaerer 2003; Thuan & Izotov 2005) as is expected in primeval galaxies in the early universe. These first stars (population III stars) should be very massive and hot (e.g., Abel et al. 2002), emitting very hard ionizing radiation, thus very effective in ionizing hydrogen and helium, then strong He II emis-

sion lines are likely present in the spectra of these galaxies (e.g., Schaerer 2002, 2003). Originally, the low abundances of heavy elements in H II/BCD galaxies and the non-detection of an old stellar population have given rise to the question of whether they may be presently forming their first generation of stars (Sargent & Searle 1970). Recent works, however, have shown that most H II galaxies seem to present an underlying population of old stars from previous episodes of SF (e.g., Papaderos et al. 1996; Telles & Terlevich 1997; Cairós et al. 2003) suggesting an intermittent SF history with short intense SF episodes followed by long quiescent phases.

To date, a small but an increasing number of H II/BCD galaxies has been observed using Integral Field Unit (IFU) spectroscopy (e.g., Izotov et al. 2006a; Lagos et al. 2009; Cairós et al. 2009a,b, 2010; Monreal-Ibero et al. 2010) in order to study the spatial distribution of their properties (i.e., emission lines, extinction, kinematics, abundances). In

\* E-mail: plagos@astro.up.pt

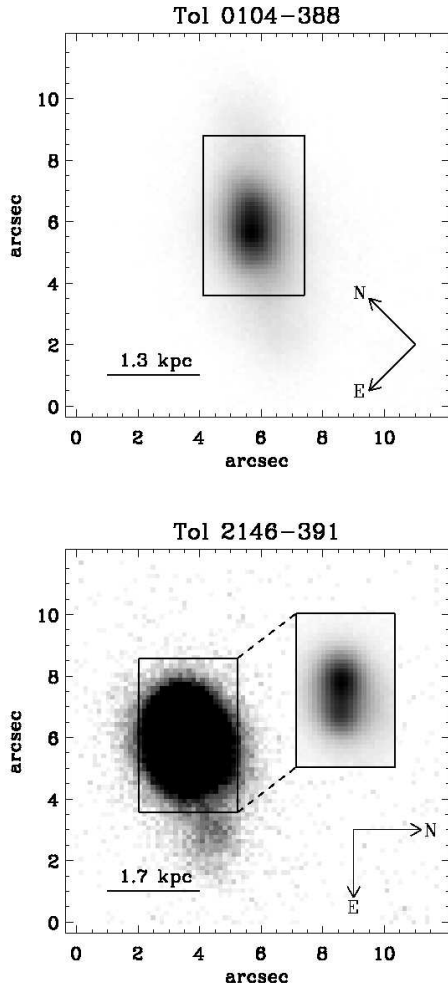


**Figure 1.** g-band acquisition image of the galaxies Tol 0104-388 and Tol 2146-6391 in logarithmic scale. The rectangle indicates the GMOS-IFU FoV of  $3''.5 \times 5''$ .

particular, some of these studies have shown a remarkable chemical homogeneity of oxygen abundance in BCD galaxies (e.g., Lagos et al. 2009). This implies that oxygen and all  $\alpha$ -elements are primary, produced by massive stars ( $>8-10 M_{\odot}$ ) and released into the interstellar medium (ISM) during their supernova (SN) phase. These newly synthesized metals will be dispersed in the whole galaxy and mixed via hydrodynamic mechanisms in timescales of few  $10^8$  yr. On the other hand, the ratio N/O was also found to be rather constant for BCD galaxies ( $\log(N/O) \simeq -1.6$ ; Edmunds & Pagel 1978; Alloin et al. 1979; Izotov & Thuan 1999), implying mainly primary production of nitrogen at low metallicity ( $12 + \log(O/H) \leq 7.6$ ), although the amount coming from each source, primary or secondary, is still debated because of the lack of a clear mechanism that produces N in massive stars besides the effect of the stellar rotation (Meynet & Maeder 2005). The observed spread of N/O at  $7.6 \leq 12 + \log(O/H) \leq 8.3$  is seen to be large and has been attributed to observational uncertainties, a loss of heavy elements via galactic winds (van Zee et al. 1998) and/or to the time delays (delayed-release hypothesis) between the pro-

duction of oxygen by massive stars and that of nitrogen by intermediate and/or massive stars. In this scenario the SF is an intermittent process in H II/BCD galaxies (Garnett 1990) with several SF bursts. However, the delayed-release scenario cannot explain the presence of H II/BCD galaxies with high N/O ratio in comparison to the expected value for their O content. The most plausible explanation of the high N/O ratio observed in these objects is the chemical pollution of N due to the presence of Wolf-Rayet (WR) stars (e.g., López-Sánchez & Esteban 2010a). Localized nitrogen self-enrichment has been measured in a few cases (e.g., Kobulnicky et al. 1997, in NGC 5253) and attributed to the release of N into the ISM by the action of strong winds produced by these stars. Although, there are a few BCD galaxies with significant variations of oxygen abundance, such as in two H II regions of Haro 11 ( $12 + \log O/H = 8.33 \pm 0.01$  in Haro B and  $12 + \log O/H = 8.10 \pm 0.04$  in Haro C; Guseva et al. 2012), no localized oxygen enrichment systems have been confirmed (Lagos et al. 2009). Finally, at high metallicity ( $12 + \log(O/H) \geq 8.3$ ) the N/O ratio clearly increases with increasing oxygen abundance. Hence, nitrogen is essentially a secondary element in this metallicity regime.

The origin of hard-ionization emission lines such as He II  $\lambda 4686$  in BCD galaxies has been a subject of study in recent years given that photoionized models of H II regions fail to reproduce the observed high-ionization line ratios. In particular, the observed intensity of He II  $\lambda 4686$  with respect to H $\beta$  is several orders of magnitude larger than model predictions for photoionized regions (Stasińska 1990). Several mechanisms for producing hard ionizing radiation have been proposed, such as massive main-sequence stars (Schaerer & de Koter 1997), WR stars (Schaerer 1996), primordial zero-metallicity stars (Schaerer 2002, 2003), high-mass X-ray binaries (HMXBs; Garnett et al. 1991), radiative shocks (Dopita & Sutherland 1996) and O stars at low metallicity may also contribute to the He II ionizing flux (Brinchmann et al. 2008). Fricke et al. (2001) and Izotov et al. (2001, 2004) have explored these different mechanisms which can produce the hard radiation in SBS 0335-052, Tol 1214-277 and Tol 65. They concluded that the ionization produced by main-sequence stars cannot explain the strong [Fe V]  $\lambda 4227$  and He II  $\lambda 4686$  emission lines, but other ionization sources as WR stars, HMXB systems and fast shocks, can be considered.

We focus here on two compact H II galaxies: Tol 0104-388 and Tol 2146-391 in order to study the relationship between the physical-chemical and kinematics properties, the nature of their hard ionization radiation pattern (He II  $\lambda 4686$  emission lines) in the ISM of these galaxies based on IFU spectroscopic observations on the Gemini South telescope. We selected these galaxies because both objects belong to a subset sample of H II galaxies with compact morphology and relative low metallicity ( $12 + \log(O/H) \lesssim 7.8-7.9$  dex), possibly mimicking the properties one expects for young galaxies at high redshift. In Fig. 1 we show g-band acquisition images of the galaxies Tol 0104-388 and Tol 2146-391. With the present observations, we note that Tol 2146-391 encompasses two main giant H II regions (GH IIRs), as shown in Fig. 1. While Tol 0104-388 shows one GH IIR. In Table 1 we show the general parameters of these galaxies.

This paper is organized as follows: the observations and data reduction are presented in Sect. 2. In Sect. 3 we show

**Table 1.** General parameters of the galaxies.

Name	Coordinates (J2000)		D (3K CMB) <sup>a</sup>	1''(3K CMB)	12+log(O/H) <sup>b</sup>	Other names
Tol 0104-388	01:07:02.1	-38:31:52	88.4	429	8.02	CTS 1001
Tol 2146-391	21:49:48.2	-38:54:09	117.3	569	7.82	

<sup>a</sup> Obtained from NED.

<sup>b</sup> Derived from the present observations.

our results based in the study of the detected emission lines. In Sect. 4 we discuss our results and in Sect. 5 we summarize our conclusions.

## 2 OBSERVATIONS AND DATA REDUCTION

The observations were performed with the Gemini Multi-Object Spectrograph GMOS (Hook et al. 2004) and the IFU unit (Allington-Smith et al. 2002, hereafter GMOS–IFU) at Gemini South Telescope in Chile, using the grating B600+<sub>-</sub>G5323 (B600) and grating R600+<sub>-</sub>G5324 (R600) in one slit mode. The GMOS-IFU in one slit mode composes a pattern of 750 hexagonal elements with a projected diameter of 0''.2, covering a total 3''.5 × 5'' field of view (FoV), where 250 of these elements are dedicated to sky observation. The CCD detector is assembled by 3 chips with two small gaps. The data were obtained in two different nights with seeing that range values from ~0''.7 to ~0''.9 obtained from the FWHM of stars in acquisition images. Table 2 summarizes our observations.

Data reduction was carried out using the Gemini software package version 1.9 inside IRAF<sup>1</sup>. This includes bias subtraction, flat-field correction, wavelength calibration and sky subtraction. The flux calibration was performed using the sensitive function derived from observation of the stars EG 21 and H 600. The 2D data images were transformed into 3D data cubes, resampled as square pixels with 0''.2 spatial resolution and corrected for differential atmospheric refraction (DAR) using the *gfcube* routine. Finally, the data cubes obtained using the gratings B600 and R600 were combined, for each galaxy, forming a final data cube covering a total spectral range from ~3021 to 7225 Å. More details about the reduction procedure applied to our data can be found in Lagos et al. (2009).

Figure 2 shows the integrated spectrum of the galaxies summing over all spaxels in the FoV. In this figure we identified the main emission lines detected and used in our study. The spectral resolution ( $R_{B600}=1688$  and  $R_{R600}=3744$ ) of the GMOS–IFU using gratings B600 and R600 allows us to resolve the [O II]  $\lambda\lambda 3726/29$  doublet, [O III]  $\lambda 4363$  and other weak emission lines. The most remarkable feature in the spectrum of these galaxies is the detection of He II  $\lambda 4686$  that are associated with a high-ionization radiation. We detect, for the first time, very weak He II  $\lambda 4686$  emission line in the spectrum of Tol 0104-388. While in Tol 2146-391

the presence of this high ionization emission line has been measured previously in the literature (e.g., Papaderos et al. 2006; Guseva et al. 2007, 2011).

Finally, the emission line fluxes were measured using the IRAF task *fitprofs* by fitting Gaussian profiles. Since most of the emission lines were measured using an automatic procedure, we filtered the maps assigning the value 0 erg cm<sup>-2</sup> s<sup>-1</sup> to all spaxels with signal to noise ratio (S/N) < 3. The error associated with each emission line ( $\sigma_i$ ) was calculated using that  $\sigma_i = \sigma_c N^{1/2} \sqrt{1 + EW/N\Delta}$ , where  $\sigma_c$  is the standard deviation in the local continuum associated with each emission line, N is the number of pixels, EW is the equivalent width of the line, and  $\Delta$  is the instrumental dispersion in Å (see Lagos et al. 2009).

## 3 PROPERTIES OF THE IONIZED GAS

### 3.1 Emission lines, EW(H $\beta$ ) and extinction

We used the flux measurement procedure described previously in Sect. 2 to construct emission line maps (e.g., [S II]  $\lambda 6731$ , [S II]  $\lambda 6717$ , [N II]  $\lambda 6548$ , [N II]  $\lambda 6584$ , H $\alpha$ , [O III]  $\lambda 5007$ , [O III]  $\lambda 4959$ , H $\beta$ , He II  $\lambda 4684$ , [O III]  $\lambda 4363$ , H $\gamma$ , [O II]  $\lambda 3726, 29$ , continuum) in a FoV of 3''.2 × 5'', equivalent to ~1372 pc × 2058 pc for Tol 0104-388 and ~1820 pc × 2730 pc for Tol 2146-391. In Fig. 3 we show the [O III]  $\lambda 4363$ , H $\alpha$ , [N II]  $\lambda 6586$  emission line maps and continuum near H $\alpha$  of Tol 0104-388 (upper maps) and Tol 2146-391 (lower maps), respectively. The flux map of these emission lines displays a single peak in Tol 0104-388 but the elongated shape of Tol 2146-391 suggests a double peak as is noted in the acquisition image of Fig. 1. Unfortunately, we did not resolve spatially these two GH IIRs in our monochromatic maps from the data cube of Tol 2146-391.

The observed emission line fluxes, for all the spaxels in our FoV, have been corrected for extinction using the observed Balmer decrement as  $I(\lambda)/I(H\beta) = F(\lambda)/F(H\beta) \times 10^{c(H\beta)f(\lambda)}$ , using the Cardelli et al. (1989) reddening curve,  $f(\lambda)$ . The observed  $F(\lambda)$  and corrected emission line fluxes  $I(\lambda)$  relative to the H $\beta$  multiplied by a factor of 100 and their error, the observed flux of the H $\beta$  emission line, the H $\beta$  equivalent widths EW(H $\beta$ ) and the extinction coefficient  $c(H\beta)$  for the integrated galaxy are given in Table 3.

In Fig. 4 we show the spatial distribution of EW(H $\beta$ ) and extinction  $c(H\beta)$  for our sample galaxies. The EW(H $\beta$ ) in Tol 0104-388 varies from ~0 Å to 200 Å and in Tol 2146-391 varies from ~0 Å to 386 Å. While, the  $c(H\beta)$  extinction varies from 0 to ~0.66 in Tol 0104-388 and from 0 to ~1.33 in Tol 2146-391. The EW(H $\beta$ ) and extinction distribution  $c(H\beta)$  in these galaxies shows an inhomogeneous pattern,

<sup>1</sup> IRAF is distributed by NOAO, which is operated by the Association of Universities for Research in Astronomy Inc., under cooperative agreement with the National Science Foundation.

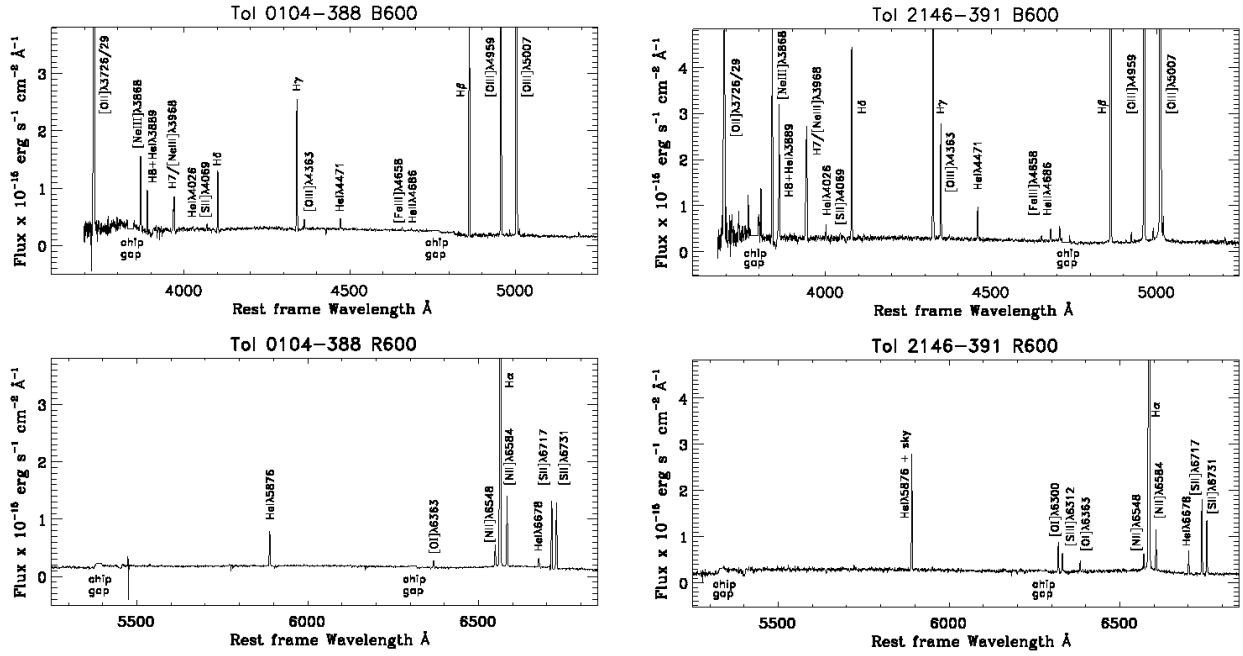


**Figure 2.** Integrated spectra (summing over all spaxels in the FoV) of Tol 0104-388 and Tol 2146-391. Top panels: blue spectrum (B600 grating), Bottom panels: red spectrum (R600 grating). The gaps between the detectors are shown in the figure.

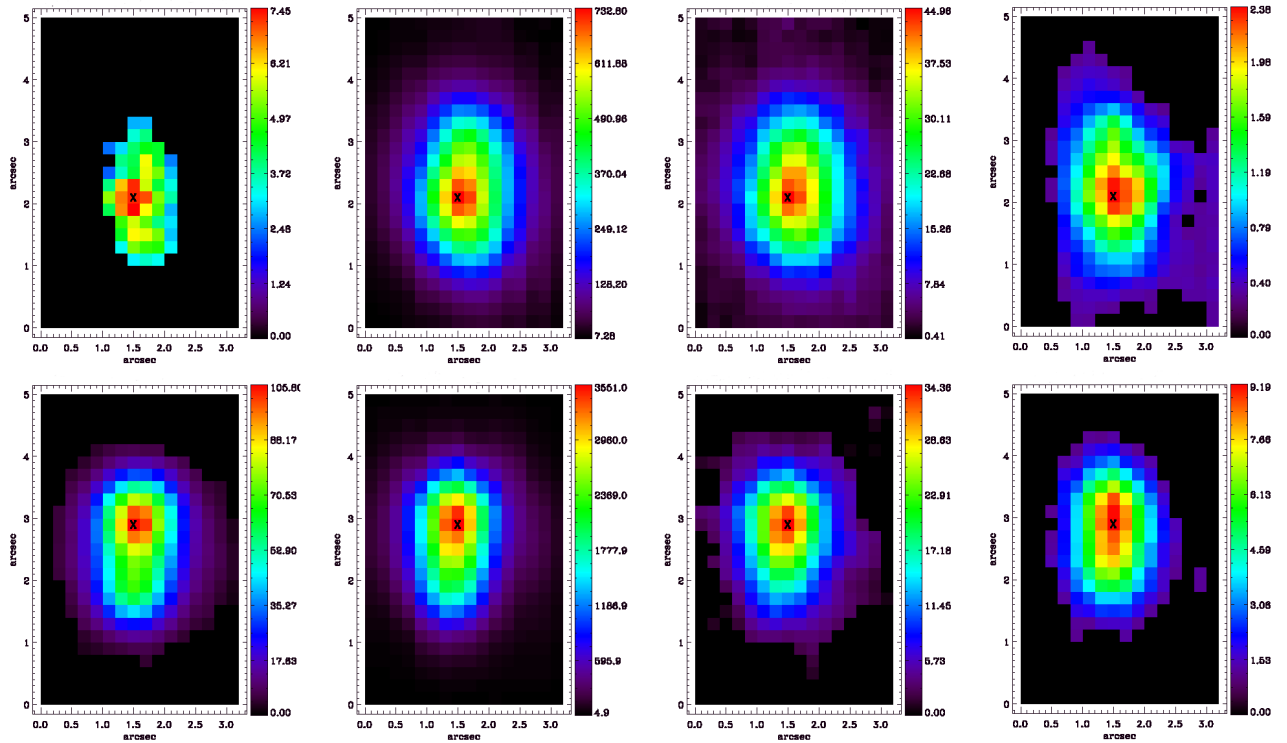


**Figure 3.** Observed emission line maps (from the left to the right)  $[O\text{ III}]\lambda 4363$ ,  $H\alpha$ ,  $[N\text{ II}]\lambda 6584$ , and  $H\alpha$  continuum of Tol 0104-388 (upper panels;  $1''=429$  pc) and Tol 2146-391 (lower panels;  $1''=569$  pc) in the original  $0''.2$  pixel size. Fluxes in units of  $10^{-18}$  ergs  $\text{cm}^{-2}$   $\text{s}^{-1}$  and continuum in units of  $10^{-18}$  ergs  $\text{cm}^{-2}$   $\text{s}^{-1}$   $\text{\AA}^{-1}$ . The maximum  $H\alpha$  emission is indicated in the maps by an X symbol.

**Table 2.** Observing log.

Name	Grating	Date	Exp. time (s)	Airmass <sup>a</sup>	Seeing <sup>b</sup> (")
Tol 0104-388	B600	2004-12-31	3×1800	1.45	0.69
	R600	2005-10-07	3×2400	1.03	0.86
Tol 2146-391	B600	2005-08-11	3×1800	1.19	0.91
	R600	2004-09-20	2×2400	1.02	0.82

<sup>a</sup> Obtained from the average values of the different exposure.

<sup>b</sup> The seeing was obtained as the FWHM of stars in acquisition images.

**Table 3.** Observed and extinction corrected emission lines for Tol 0104-388 and Tol 2146-391. The fluxes are relative to F(Hβ)=100.

	Tol 0104-388		Tol 2146-391	
	F(λ)/F(Hβ)	I(λ)/I(Hβ)	F(λ)/F(Hβ)	I(λ)/I(Hβ)
[OII] λ3726	76.00±2.08	96.37±5.29	18.84±2.31	23.54±2.76
[OII] λ3729	105.30±3.30	133.47±8.37	25.72±0.23	32.12±0.27
[NeIII] λ3868	23.80±0.99	29.50±2.45	28.98±1.28	35.44±1.50
H8+He I λ3889	13.20±0.51	16.30±1.27	13.00±0.40	15.84±0.97
[NeIII] λ3968	6.80±0.53	8.27±1.28	9.46±0.16	11.51±0.39
H7 λ3970	9.26±0.50	11.26±1.23	9.76±0.13	11.88±0.32
He I λ4026	1.37±0.30	1.65±0.72	1.18±0.07	1.40±0.17
[SII] λ4069	2.09±0.25	2.49±0.59	0.85±0.58	1.00±0.66
Hδλ4101	19.80±2.90	23.45±6.88	19.02±1.04	22.29±1.18
Hγλ4340	42.60±2.13	47.81±4.78	40.76±2.07	45.42±2.26
[OIII] λ4363	3.60±0.20	4.02±0.45	10.78±0.63	11.95±0.68
He I λ4471	3.63±0.11	3.95±0.25	3.22±0.09	3.49±0.19
[FeIII] λ4658	1.38±0.05	1.44±0.11	0.67±0.04	0.70±0.08
He II λ4686	0.80±0.09	0.83±0.18	1.56±0.52	1.61±0.53
Hβλ4861	100.00±3.70	100.00±3.70	100.00±2.38	100.00±2.38
[OIII] λ4959	119.33±5.23	117.09±5.13	202.90±4.09	199.33±4.03
[OIII] λ5007	353.33±17.69	343.64±17.20	610.51±10.47	594.79±10.25
He I λ5876	12.27±0.36	10.56±0.62	...	...
[OI] λ6300	...	...	2.83±0.40	2.36±0.67
[SIII] λ6312	...	...	1.62±0.06	1.35±0.10
[OI] λ6363	2.72 ±0.24	2.23±0.39	0.95±0.03	0.79±0.05
[NII] λ6548	7.93±1.05	6.38±0.84	1.90±0.25	1.55±0.21
Hαλ6563	370.00±10.06	297.15±8.08	362.32±7.22	295.00±6.12
[NII] λ6584	25.20±1.60	20.20±1.28	3.86±0.42	3.14±0.35
He I λ6678	3.59 ±0.16	2.85±0.25	2.06±0.06	1.66±0.10
[SII] λ6717	25.20±1.68	19.94±1.33	7.06±0.91	5.67±0.76
[SII] λ6731	24.86±1.64	19.64±1.29	5.22±0.81	4.18±0.68
F(Hβ) <sup>a</sup>	15.00±0.28		55.20±0.61	
EW(Hβ) <sup>b</sup>	109±22		229±30	
c(Hβ)	0.32		0.30	

<sup>a</sup> In units of  $\times 10^{-15}$  erg cm<sup>-2</sup> s<sup>-1</sup>

<sup>b</sup> In units of Å

where the peak of these values are displaced from the maximum of Hα emission. In particular, the extinction map of Tol 2146-391 shows a hole-like structure in the right part of the FoV, where several spaxels located in this regions shows values close to 0 or F(Hα)/F(Hβ)~2.87. These structures appear to be real given that are not produced by misalignment between the maps.

We compared our integrated extinction value of

c(Hβ)=0.32, in Tol 0104-388, that is in reasonable agreement with those derived with long slit spectroscopy of 0.30 by Peña et al. (1991) and 0.39 by Telles, Melnick & Terlevich (1997). The integrated He II λ4686 emission in Tol 0104-388 is very weak and corresponds to  $\lesssim 1\%$  of the observed Hβ flux. In the case of Tol 2146-391, we obtained an integrated extinction c(Hβ)= 0.30 that differs slightly from the value obtained by Guseva et al. (2007) of 0.18, 0.20 by

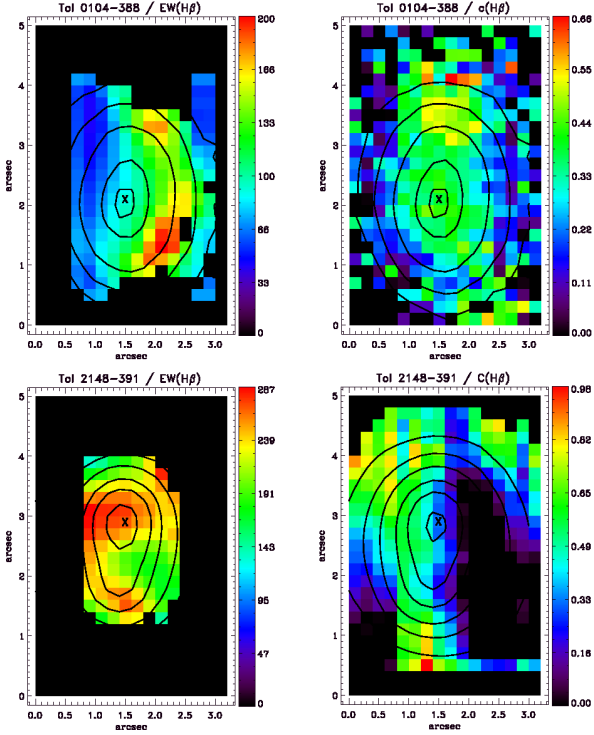


**Figure 4.** Spatial distribution of  $\text{EW}(\text{H}\beta)$  and  $c(\text{H}\beta)$  for our sample galaxies. The maximum  $\text{H}\alpha$  emission is indicated in the maps by an X symbol.  $\text{H}\alpha$  emission line contours are overlotted on all maps.

Papaderos et al. (2006) and 0.12 by Kehrig et al. (2006), but agrees with the value found by Guseva et al. (2011) of 0.30 for the eastern and 0.32 for the western H II regions, respectively. The integrated  $\text{He II } \lambda 4686$  emission in Tol 2146-391 corresponds to  $<2\%$  of the observed  $\text{H}\beta$  flux. Our intensity value of  $I(\text{He II } \lambda 4686)/I(\text{H}\beta)=0.016\pm 0.005$ , in this galaxy, agrees within the errors with the value of  $I(\text{He II } \lambda 4686)/I(\text{H}\beta)=0.017\pm 0.010$  obtained by Papaderos et al. (2006),  $0.022\pm 0.001$  by Guseva et al. (2007) and  $0.017\pm 0.001$  for the western and  $0.023\pm 0.001$  for the eastern GH IIRs by Guseva et al. (2011).

Finally, we estimated the mean age of the starburst in each one of the galaxies comparing the integrated  $\text{EW}(\text{H}\beta)=109 \text{ \AA}$  for Tol 0104-388 and  $\text{EW}(\text{H}\beta)=229 \text{ \AA}$  for Tol 2146-391 with STARBURST99 (Leitherer et al. 1999). We assumed an instantaneous burst, a metallicity of  $Z=0.004$  and a Kroupa IMF ( $\propto M^{-\alpha}$ ) with  $\alpha=1.3$  for stellar masses between 0.1 to  $0.5M_{\odot}$  and  $\alpha=2.3$  for masses between 0.5 and  $100M_{\odot}$ . Thus, the estimated mean age in the FoV of the galaxies is  $\sim 5$  Myr in Tol 0104-388 and  $\sim 4$  Myr in Tol 2146-391.

### 3.2 Velocity field

We have obtained the spatial distribution of radial velocity  $v_r$  by fitting a single Gaussian to the  $\text{H}\alpha$  emission line profiles. In order to better examine the variations in the FoV, in Fig. 5 we show the smoothed radial velocity derived from the shifts of the  $\text{H}\alpha$  line peak.

The velocity field  $v_r$  of Tol 0104-388 in the left panel

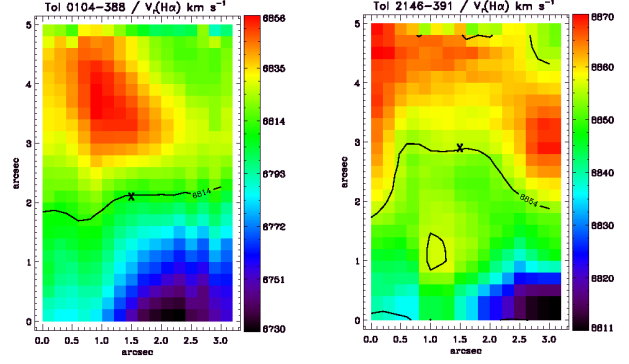


**Figure 5.**  $\text{H}\alpha$  radial velocity in units of  $\text{km s}^{-1}$ . The maximum  $\text{H}\alpha$  emission is indicated in the maps by an X symbol. The black contours in the radial velocity maps correspond to the systemic velocity.

of Fig. 5 shows an apparent systemic motion where the upper part of the galaxy is redshifted, while the lower part is blueshifted, with a relative motion of  $\sim 50 \text{ km s}^{-1}$  with respect to the systemic velocity (black contour in the radial velocity map). This velocity map indicates the presence of a clear rotation pattern in this galaxy. On the other hand, the radial velocity map of Tol 2146-391 (right panel of Fig. 5) is rather complex indicating asymmetric gas motions without any clear rotational pattern. The whole range of radial velocities displayed in the map is about  $60 \text{ km s}^{-1}$ . No significant differences were found from the map derived using  $\text{H}\beta$  and  $[\text{O III}]\lambda 5007$  in both galaxies.

The systemic velocity obtained from the fit to the emission maxima (located on the cross in the velocity maps) is  $6803 \text{ km s}^{-1}$  for Tol 0104-388 and  $8854 \text{ km s}^{-1}$  for Tol 2146-391. For the integrated spectrum of the galaxies we obtained values of  $6815 \text{ km s}^{-1}$  for Tol 0104-388 and  $8854 \text{ km s}^{-1}$  for Tol 2146-391, respectively. Although our GMOS-IFU observations were performed using the medium resolution grating, we found a velocity dispersion<sup>2</sup> of  $\sigma(\text{H}\alpha)\simeq 44 \text{ km s}^{-1}$  in Tol 0104-388 and  $\sim 25 \text{ km s}^{-1}$  in Tol 2146-391 assuming a simple Gaussian profile. These results are in agreement with the integrated values obtained by Bordalo & Telles (2011) with  $\sigma(\text{H}\alpha)=48.2\pm 0.4 \text{ km s}^{-1}$  in Tol 0104-388 and  $\sigma(\text{H}\alpha)=25.6\pm 0.4 \text{ km s}^{-1}$  in Tol 2146-391, using the high dispersion spectrograph FEROS at ESO.

### 3.3 Emission Line Diagnostic Diagrams

The standard diagnostic diagrams BPT (Baldwin et al. 1981) have been used to analyze the possible excitation mechanisms present in Tol 0104-388 and Tol 2146-391. Fig. 6 considers:  $[\text{O III}]\lambda 5007/\text{H}\beta$  versus  $[\text{S II}]\lambda\lambda 6717,6731/\text{H}\alpha$  and  $[\text{O III}]\lambda 5007/\text{H}\beta$  versus  $[\text{N II}]\lambda 6584/\text{H}\alpha$  for both galaxies in our sample. The solid lines (adapted from Osterbrock & Ferland 2006) show the locus of separation

<sup>2</sup> We derived the velocity dispersion using the relationship  $\sigma^2=\sigma_{obs}^2-\sigma_{inst}^2-\sigma_{th}^2$ . We used a value of  $33.4\pm 1.0 \text{ km s}^{-1}$  for the instrumental dispersion and  $\sigma_{th}=\sqrt{kT_e/m_H}\approx 10 \text{ km s}^{-1}$  and  $11 \text{ km s}^{-1}$  for thermal broadening considering  $T_e=12199 \text{ K}$  and  $15277 \text{ K}$  for Tol 0104-388 and Tol 2146-391, respectively.

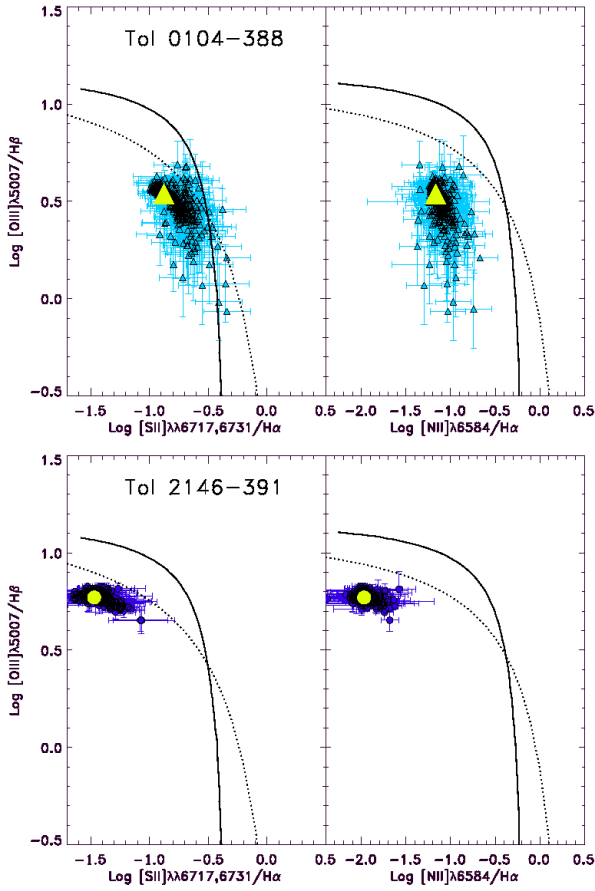


**Figure 6.** Position of the individual  $0''.2$  spaxels in Tol 0104-388 (upper panels) and Tol 2146-391 (lower panels) in the BPT diagnostic diagrams. The solid curves show the empirical borders found by Osterbrock & Ferland (2006), while the dotted lines show the theoretical borders proposed by Kewley et al. (2001). The grey filled circles and triangles mark the integrated values of the galaxies.

between regions dominated solely by photoionization (H II-like regions) and regions dominated by shocks (e.g., AGNs). The dotted line represents the same as the solid line but using the models given by Kewley et al. (2001). This figure shows that the position of all individual spaxels, in these diagrams, suggest that photoionization from stellar sources is the dominant excitation mechanism in our two galaxies.

In Fig. 7 we show the maps for the three available line ratios involved in these diagrams  $[\text{O III}]\lambda 5007/\text{H}\beta$ ,  $[\text{S II}]\lambda\lambda 6717,6731/\text{H}\alpha$  and  $[\text{N II}]\lambda 6584/\text{H}\alpha$ . This figure shows that the ionization structure in the central region of Tol 0104-388 is rather constant for  $[\text{N II}]\lambda 6584/\text{H}\alpha$ . While  $[\text{O III}]\lambda 5007/\text{H}\beta$  and  $[\text{S II}]\lambda\lambda 6717,6731/\text{H}\alpha$  do not show a uniform distribution. The same behavior is observed in Tol 2146-391. The spatial structure changes from the peak of  $\text{H}\alpha$  emission to the outer part of the galaxies. Comparing the two galaxies, we can see that the data points of Tol 2146-391, in Fig 6, are more highly clustered to the upper left of the diagram than those of Tol 0104-388. These features usually indicate a harder ionization field either by young star clusters or star cluster complexes at lower metallicities. Finally, our integrated  $[\text{S II}]\lambda\lambda 6717,6731/\text{H}\alpha$  and  $[\text{N}$

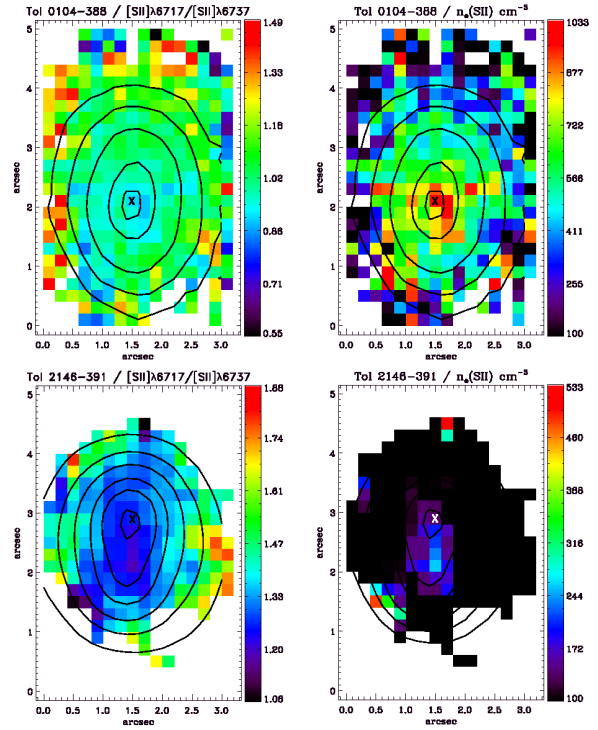


**Figure 8.**  $[\text{S II}]\lambda 6717/[\text{S II}]\lambda 6731$  ratio maps and electron density maps  $n_e(\text{S II}) \text{ cm}^{-3}$  of Tol 0104-388 (upper panels) and Tol 2146-391 (lower panels). The maximum  $\text{H}\alpha$  emission is indicated in the maps as X symbol.  $\text{H}\alpha$  contours are overlapped on the maps.

$\text{II}]\lambda 6584/\text{H}\alpha$  values are consistent with the ones reported in the literature by Guseva et al. (2011) in Tol 2146-391 and inferred using the emission lines reported by Kehrig et al. (2006) in Tol 0104-388.

### 3.4 Chemical abundances

The first step in the abundance derivation is the calculation of the electron temperature and density. We calculated the electron temperature  $T_e(\text{O III})$  from the ratio  $[\text{O III}]\lambda\lambda 4959,5007/[\text{O III}]\lambda 4363$  and the electron density from  $[\text{S II}]\lambda 6717/[\text{S II}]\lambda 6731$  ratio using the five level atomic model FIVEL (De Robertis et al. 1987), implemented under the IRAF STS package *nebular*.

Fig. 8 shows the spatial distribution of the  $[\text{S II}]\lambda 6717/[\text{S II}]\lambda 6731$  ratio and the electron density, and Fig. 9 shows the electron temperature  $T_e(\text{O III})$  obtained from the  $[\text{O III}]\lambda\lambda 4959,5007/[\text{O III}]\lambda 4363$  ratio, for both galaxies in our sample.

The oxygen, nitrogen, neon and sulfur abundances were calculated as

$$\frac{\text{O}}{\text{H}} = \frac{\text{O}^+}{\text{H}^+} + \frac{\text{O}^{+2}}{\text{H}^+}, \quad (1)$$

$$\frac{\text{N}}{\text{H}} = \text{ICF}(\text{N}) \frac{\text{N}^+}{\text{H}^+}, \quad (2)$$

$$\frac{\text{Ne}}{\text{H}} = \text{ICF}(\text{Ne}) \frac{\text{Ne}^{+2}}{\text{H}^+}, \quad (3)$$

$$\frac{\text{S}}{\text{H}} = \text{ICF}(\text{S}) \left( \frac{\text{S}^+}{\text{H}^+} + \frac{\text{S}^{+2}}{\text{H}^+} \right), \quad (4)$$

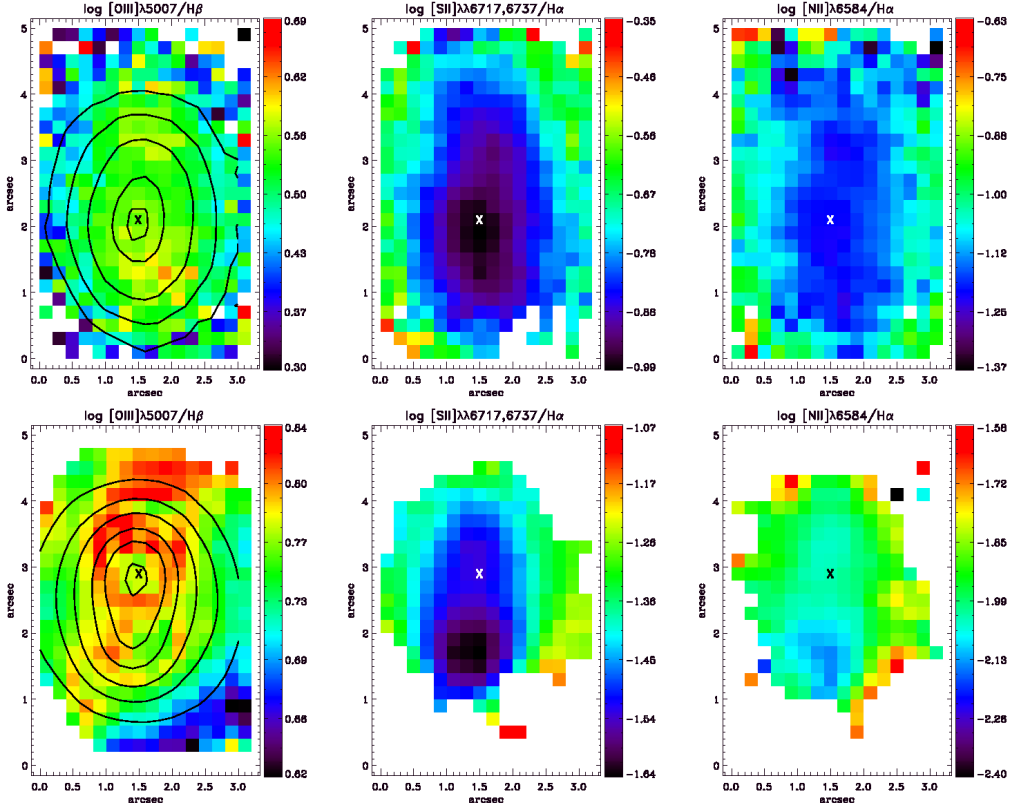


**Figure 7.** Emission line ratios:  $\log [\text{O III}]\lambda 5007/\text{H}\beta$ ,  $\log [\text{S II}]\lambda\lambda 6717, 6737/\text{H}\alpha$  and  $\log [\text{N II}]\lambda 6584/\text{H}\alpha$  for both galaxies in our sample (Tol 0104-388: upper panels and Tol 2146-391: lower panels). The maximum  $\text{H}\alpha$  emission is placed over region A and is indicated in the maps by an X symbol.

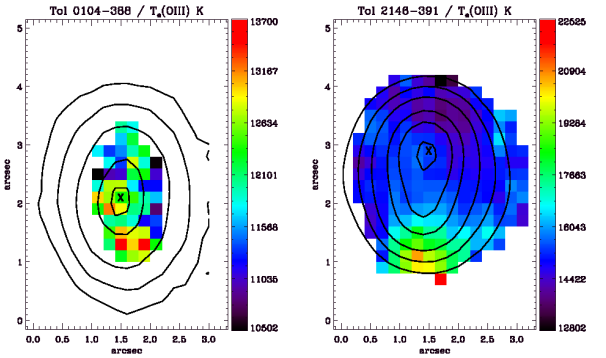


**Figure 9.** Electron temperature maps in K of Tol 0104-388 (upper panel) and Tol 2146-391 (lower panel) obtained from  $[\text{O III}]\lambda\lambda 4959, 5007/[\text{O III}]\lambda 4363$  emission line ratio. The maximum  $\text{H}\alpha$  is indicated in the maps by a X symbol.  $\text{H}\alpha$  contours are overlotted on the maps.

where  $\text{O}^+$ ,  $\text{O}^{+2}$ ,  $\text{N}^+$ ,  $\text{Ne}^{+2}$  and  $\text{S}^+$  ions are obtained from the *nebular* output file. Nitrogen, neon and sulfur abundances were calculated using ionization correlation factors (ICF) and the relationship between  $\text{S}^+$  and  $\text{S}^{+2}$  given by Kingsburgh & Barlow (1994). We assumed that  $T_e(\text{O II})$  temperature is given by  $T_e(\text{O II}) = 2/(T_e^{-1}(\text{O III}) + 0.8)$  (Pagel et al. 1992),  $T_e(\text{S III}) = 0.83 \times T_e(\text{O III}) + 0.17$  (Garnett 1992) and  $T_e(\text{O II}) = T_e(\text{S II}) = T_e(\text{N II})$ . In Table 4 we show the electron density, temperature and abun-

dances calculated for each one of the integrated apertures considered in this study. Fig. 10 (left panel) shows the spatial distribution of the oxygen abundances in the spaxels where the emission lines  $[\text{O III}]\lambda 4363$  and  $[\text{O II}]\lambda\lambda 3726/29$  were detected, and in the right panel of the same fig. we show the spatial distribution of  $\text{N}^+$  in the spaxels where  $[\text{N II}]\lambda 6584$  was detected. Finally, in Fig. 11 we show the spatial distribution of  $\log(\text{N}/\text{O})$ .

*Tol 0104-388.* In this galaxy, the electron density is relatively high (upper panel of Fig. 8), varying from  $\sim 100$  to  $1033 \text{ cm}^{-3}$ , while the temperature varies from 10502 K to 13700 K. The highest values of density are placed near the peak of  $\text{H}\alpha$  emission. We obtained an integrated electron temperature of  $T_e(\text{O III}) = 12199 \pm 412 \text{ K}$ , that agree with the value reported by Peña et al. (1991) of  $1.25 \pm 0.15 \times 10^4 \text{ K}$ , and a density of  $n_e(\text{S II}) = 614 \text{ cm}^{-3}$ . The oxygen abundance values in units of  $12 + \log(\text{O}/\text{H})$  in Tol 0104-388 range from 7.96 to 8.24, with a mean value of 8.06 and a standard deviation of 0.06. We obtained an integrated value of  $12 + \log(\text{O}/\text{H}) = 8.02 \pm 0.04$  that agrees with the mean value of the spaxels within the errors. This integrated  $12 + \log(\text{O}/\text{H})$  abundance is consistent with the value of  $12 + \log(\text{O}/\text{H}) = 8.19 \pm 0.15$  derived by Peña et al. (1991). The  $\text{N}^+/\text{H}^+$  distribution range values from  $1.85 \times 10^{-6}$  to  $2.72 \times 10^{-6}$  with a mean value of  $2.21 \times 10^{-6}$ . With this information we found that the  $12 + \log(\text{N}/\text{H})$  range values from 6.60 to 6.92, a mean value of 6.74, a standard deviation of 0.07 and an integrated value of  $12 + \log(\text{N}/\text{H}) = 6.77 \pm 0.08$ .



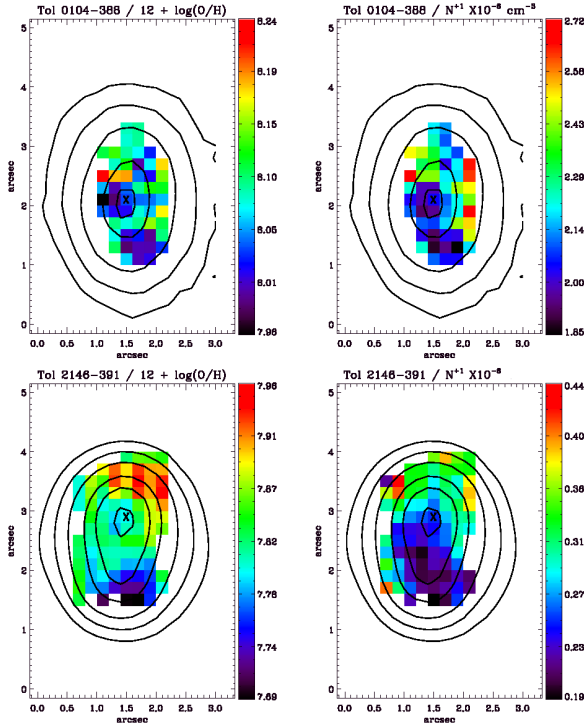


**Figure 10.**  $12+\log(\text{O}/\text{H})$  abundance and  $\text{N}^+/\text{H}^+$  ratio maps of Tol 0104-388 (upper panels) and Tol 2146-391 (lower panels). Overlaid are the  $\text{H}\alpha$  flux contours. The maximum  $\text{H}\alpha$  emission is indicated in the maps by an X symbol.

Finally, the  $\log(\text{N}/\text{O})$  ratio range values from -1.43 to -1.20 with a mean value of -1.33 and a standard deviation of 0.05. We found an integrated value of  $\log(\text{N}/\text{O})=-1.25\pm 0.12$ ,  $\log(\text{Ne}/\text{O})=-0.62\pm 0.23$  and  $\log(\text{S}/\text{O})=-1.70\pm 0.08$ . These values appear normal for BCD galaxies at this metallicity (Izotov & Thuan 1999; López-Sánchez & Esteban 2010a; Guseva et al. 2011).

*Tol 2146-391.* In this galaxy, we obtained an integrated temperature of  $T_e(\text{O III})=15277\pm 584$  K and a density of  $n_e(\text{S II})\lesssim 100$   $\text{cm}^{-3}$ . The electron temperature varies from 12802 K to 22525 K. The density in the outer part of the galaxy is practically constant with  $n_e(\text{S II})\lesssim 100$   $\text{cm}^{-3}$ , given that the ratio  $[\text{S II}]\lambda 6717/[\text{S II}]\lambda 6731$  is typically greater than 1 (see Fig. 8) which indicates a low density regime (Osterbrock & Ferland 2006), hence, we assumed an electron density of  $n_e\sim 100$   $\text{cm}^{-3}$  in most apertures in Tol 2146-391. Our  $n_e$  values found in the inner part of the galaxy are consistent with the values found by Guseva et al. (2011) of 162  $\text{cm}^{-3}$  and 147  $\text{cm}^{-3}$ , corresponding with the two GH IIRs (Fig. 1) found in this work. The oxygen abundance  $12+\log(\text{O}/\text{H})$  range from 7.69 to 7.96, with a mean value of 7.84 and a standard deviation of 0.06. The integrated oxygen abundance of  $12+\log(\text{O}/\text{H})=7.82\pm 0.09$  agree with the value obtained by Papaderos et al. (2006) of  $7.80\pm 0.01$ ,  $7.78\pm 0.01$  by Guseva et al. (2007) and  $7.82\pm 0.01$ - $7.79\pm 0.01$  (for the two GH IIRs) by Guseva et al. (2011) but is in disagreement with the reported value of  $7.62\pm 0.08$  given by Kehrig et al. (2006). The  $\text{N}^+/\text{H}^+$  distribution range values from  $0.19\times 10^{-6}$  to  $0.44\times 10^{-6}$  with a mean value of  $0.29\times 10^{-6}$  and a standard deviation of  $0.06\times 10^{-6}$ . Given that our calculated ICF(N), over the majority of the spaxels in the FoV, are typ-

**Table 4.** Ionic, abundances and integrated properties of Tol 0104-388 and Tol 2146-391.

	Tol 0104-388	Tol 2146-391
Te(OIII) K	12199±412	15277±584
Ne(II) $\text{cm}^{-3}$	614	$\lesssim 100$
$\text{O}^+/\text{H}^+\times 10^5$	4.16±0.11	0.62±0.04
$\text{O}^{++}/\text{H}^+\times 10^5$	6.41±0.28	6.03±0.58
$\text{O}/\text{H}\times 10^5$	10.56±0.39	6.65±0.61
$12+\log(\text{O}/\text{H})$	8.02±0.04	7.82±0.09
$\text{N}^+/\text{H}^+\times 10^6$	2.34±0.04	0.32±0.01
ICF(N)	2.54±0.16	10.67±1.62
$\text{N}/\text{H}\times 10^6$	5.94±0.48	3.43±0.69
$12+\log(\text{N}/\text{H})$	6.77±0.08	6.54±0.10
$\log(\text{N}/\text{O})$	-1.25±0.12	-1.28±0.29
$\text{S}^+/\text{H}^+\times 10^7$	2.83±0.13	0.97±0.05
$\text{S}^{++}/\text{H}^+\times 10^6$	1.67±0.10	0.71±0.08
ICF(S)	1.09±0.04	1.58±0.02
$\text{S}/\text{H}\times 10^6$	2.12±0.09	1.28±0.02
$12+\log(\text{S}/\text{H})$	6.33±0.05	6.11±0.02
$\log(\text{S}/\text{O})$	-1.70±0.08	-1.72±0.11
$\text{Ne}^{++}/\text{H}^+\times 10^5$	1.55±0.16	0.92±0.10
ICF(Ne)	1.65±0.13	1.10±0.21
$\text{Ne}/\text{H}\times 10^5$	2.55±0.50	1.01±0.32
$12+\log(\text{Ne}/\text{H})$	7.41±0.19	7.01±0.31
$\log(\text{Ne}/\text{O})$	-0.62±0.23	-0.82±0.41
He II $\lambda 4686/\text{H}\beta$	0.008±0.002	0.016±0.005
$\log([\text{O III}]\lambda 5007/\text{H}\beta)$	0.54±0.05	0.77 ±0.02
$\log([\text{N II}]\lambda 6584/\text{H}\alpha)$	-1.17±0.09	-1.97±0.12
$\log([\text{S II}]\lambda\lambda 6717,6731/\text{H}\alpha)$	-0.87±0.09	-1.47±0.16
$\sigma(\text{H}\alpha)$ $\text{km s}^{-1}$	44.47	25.75
Age Myr	4.95	4.12

ically  $\sim 10$  we found a variation of  $12+\log(\text{N}/\text{H})$  from 6.27 to 6.83, an average value of 6.52 dex and a standard deviation of 0.16. An integrated value of  $12+\log(\text{N}/\text{H})=6.54\pm 0.07$  is found in Tol 2146-391. The  $\log(\text{N}/\text{O})$  ratio range values from -1.55 to -1.05 with an average value of -1.32 and a standard deviation of 0.12. We found a value of  $\log(\text{N}/\text{O})=-1.28\pm 0.29$  summing over all spaxels in the FoV. This integrated value appear to be in agreement, within the errors, with the ones obtained by Guseva et al. (2011) for the two GH IIRs  $\log(\text{N}/\text{O})=-1.57\pm 0.03$  and  $-1.63\pm 0.03$ . Finally, our integrated  $\log(\text{Ne}/\text{O})=-0.82\pm 0.41$  appear to be consistent with values obtained by Guseva et al. (2011).

In Fig. 12 we show the distribution of  $\log(\text{N}/\text{O})$ , in Tol 0104-388 and Tol 2146-391, respectively. For each one of these two galaxies we show the integrated  $\log(\text{N}/\text{O})$  values (solid lines) and the mean  $\log(\text{N}/\text{O})$  values (dotted lines) of the data points. Table 5 summarize the statistical properties of the spaxels in our sample galaxies. We note an agreement, within the errors, between the mean value of the spaxels and the properties derived from the integrated spectrum. In the case of the oxygen abundance, we found a variation of  $\Delta(\text{O}/\text{H})\sim 0.28$  between the minimum and maximum values, for both galaxies, with a low standard deviation. This result indicates that these variations are not statistically significant across the galaxies. The  $\log(\text{N}/\text{O})$  variation in Tol 0104-388 shows a value of 0.22 with a low standard deviation. While, in Tol 2146-391 we found a variation of  $\Delta(\text{N}/\text{O})=0.50$ , with a higher standard deviation with respect to the oxygen abundance. Although the mean value of

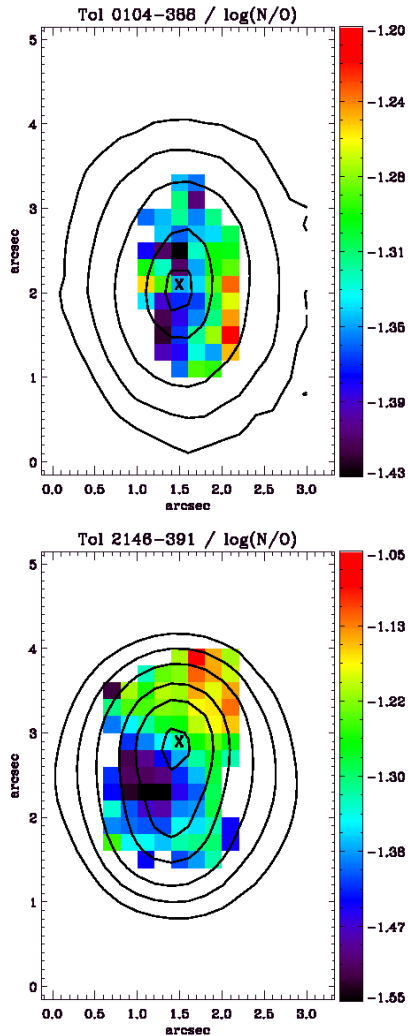


**Figure 11.**  $\log(N/O)$  ratio maps of Tol 0104-388 and Tol 2146-391. Overlaid are the  $H\alpha$  flux contours. The maximum  $H\alpha$  emission is indicated in the maps by an X symbol.

$\log(N/O)$  is consistent with the integrated value, this result indicates that a slight variation is observed in Tol 2146-391. In fact, Fig. 10 and 11 show that the  $N^+$  ions and consequently  $12+\log(N/H)$  show a slightly positive trend from the region near the  $H\alpha$  peak to the North-West part of the galaxy, producing the increasing of the  $N/O$  ratio to this direction, reaching values of  $\log(N/O) \gtrsim -1.20$ .

## 4 DISCUSSION

### 4.1 Spatial distribution and Dependence of the He II $\lambda 4686$ emission line on the $EW(H\beta)$ and metallicity of the ISM

In Fig. 13 we show the spatial distribution of He II  $\lambda 4686$  in Tol 2146-391. Fig. 14 shows the spatial distribution of  $H\beta$  emission lines in the  $0''.2$  pixel scale, for both galaxies, and superimposed in each one of the images the resampled  $0''.8$  spaxels in the region that contain the He II  $\lambda 4686$  emission line from  $4640 \text{ \AA}$  to  $4725 \text{ \AA}$ . To do this we summed the spaxels in a region of  $4 \times 4$  spaxels in order to increase the

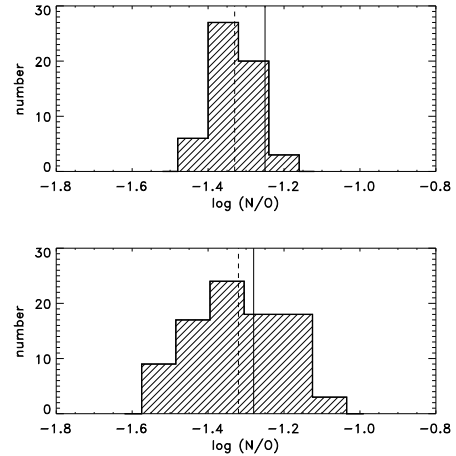


**Figure 12.** Distribution of  $\log(N/O)$ , in Tol 0104-388 (upper panel) and Tol 2146-391 (lower panel). For each of these two galaxies we show the integrated  $\log(N/O)$  values (solid lines) and the mean  $\log(N/O)$  values (dotted lines).

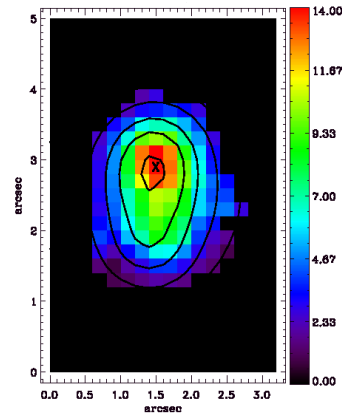


**Figure 13.** Spatial distribution of the He II  $\lambda 4686$  emission line in the galaxy Tol 2146-391. Fluxes in units of  $10^{-18} \text{ ergs cm}^{-2} \text{ s}^{-1} \text{ \AA}^{-1}$ . The maximum  $H\alpha$  emission is indicated in the map by an X symbol.

S/N. From this fig., we find a weak He II  $\lambda 4686$  emission line in the core of Tol 0104-388, previously not detected in this galaxy, so we see that in both galaxies the He II  $\lambda 4686$  emission line is concentrated in the core.

Thuan & Izotov (2005) studying a sample of galaxies where the He II  $\lambda 4686$  emission line was detected, found that the hardness of the ionizing radiation does not appear to depend on starburst age or  $EW(H\beta)$ , when the integrated properties of the galaxies are considered. On the other hand, as mentioned by previous spectroscopic studies (e.g., Campbell et al. 1986; Guseva et al. 2000; Thuan & Izotov 2005) the hardness of this ionizing radiation in BCDs increases with decreasing metallicity. This implies that these ionization emission lines are stronger in galaxies with lower metallicities. This correlation was determined from the integrate spectra of galaxies. But what is the relationship between the spatial distribution of abundances and  $EW(H\beta)$

**Table 5.** Statistical properties of the galaxies.

	Tol 0104-388			Tol 2146-391		
	Mean	SDEV <sup>a</sup>	$ \Delta^b $	Mean	SDEV	$ \Delta $
O <sup>+</sup> /H <sup>+</sup> ( $\times 10^5$ )	4.73	0.63	2.91	0.60	0.11	0.39
O <sup>++</sup> /H <sup>+</sup> ( $\times 10^5$ )	7.12	1.24	5.68	6.34	0.99	4.37
12 + log (O/H)	8.06	0.06	0.28	7.84	0.06	0.27
N <sup>+</sup> /H <sup>+</sup> ( $\times 10^6$ )	2.21	0.00	0.87	0.29	0.06	0.25
12 + log (N/H)	6.74	0.07	0.31	6.52	0.16	0.56
log (N/O)	-1.33	0.05	0.22	-1.32	0.12	0.50

<sup>a</sup> Standard deviation of the spaxels.

<sup>b</sup> Difference between minimum and maximum values.

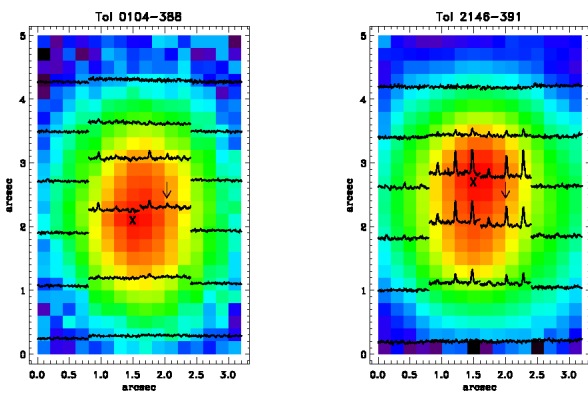


**Figure 14.** Spatial distributions of the He II  $\lambda 4686$  emission line in Tol 0104-388 and Tol 2146-391. In this figure we show the H $\beta$  emission line map in the original  $0''.2$  pixel size and superimposed the binned  $0''.8$  spaxels in the region that contain the He II  $\lambda 4686$  emission line. The maximum H $\alpha$  emission is indicated in the maps by an X symbol. The arrows in the Figures are indicating the position of He II  $\lambda 4686$  emission lines in the spectra.

with the hardness of high ionizing radiation across the spaxels in our sample galaxies?

In Fig. 15 we show the intensity of the He II  $\lambda 4686$  emission line relative to H $\beta$  of each spaxel of  $0''.2$  as a function of (a) EW(H $\beta$ ), (b) oxygen abundance 12 + log (O/H) and (c) log (N/O) ratio for the galaxy Tol 2146-391. We performed a Spearman's rank correlation test on our data in order to assess how well the relationship between He II  $\lambda 4686$  emission line can be described as a function of the other properties. From this procedure, we did not find a significant correlation between these variables using this correlation technique. In fact, the oxygen abundances appear to be uniform in the regions where the He II  $\lambda 4686$  emission line was measured. It can be interpreted that there are no correlations with small patches of the ISM.

#### 4.2 Sources of the nebular He II $\lambda 4686$ emission line and their spatial distribution

Studying a sample of GH IIRs, Guseva et al. (2000) found that galaxies with detected and nondetected WR features have the same distribution dependences of I(He II  $\lambda 4686$ )/I(H $\beta$ ) versus EW(H $\beta$ ). This implies that WR stars

are not the sole origin of He II  $\lambda 4686$  in star-forming regions. On the other hand, de Mello et al. (1998) found a spatial correlation between the nebular He II  $\lambda 4686$  emission between the star clusters and the position of WR stars in the galaxy IZw 18 supporting the hypothesis that WR stars are responsible for nebular He II emission in this galaxy. While, Izotov et al. (2006a) found that the hard ionizing radiation responsible for the He II  $\lambda 4686$  emission, in the galaxy SBS 0335-052, is not likely related with the position of the most massive and young star clusters, but rather is related to fast radiative shocks. Another possibility is that the high-ionizing radiation is produced by the accretion of gas by HMXBs (Garnett et al. 1991) located in the star cluster population in the core of the galaxies. As suggested by Thuan et al. (2004) the high X-ray luminosities of these sources may be due to a metallicity effect, resulting in a larger X-ray luminosity, so producing an additional photoionization of the gas in low-metallicity systems, as is the case of H II/BCD galaxies. Finally, Brinchmann et al. (2008) suggest that at low metallicity the main source of He II  $\lambda 4686$  ionizing photons appears to be O stars.

The action of stellar winds and supernovae (SNe) explosions from the star clusters generates expanding shells (e.g., Hodge 1974; Martin 1998) that eventually will be able to produce on large scales collisionally excited emission lines. Garnett et al. (1991) have suggested that fast radiative shocks in GH IIRs can produce relatively strong He II emission under certain conditions. Hydrodynamical models by Dopita & Sutherland (1996) have shown that fast shocks, with shock velocities of 400-500 km s<sup>-1</sup>, are an efficient means to produce a strong local UV photon field in the ISM of galaxies. Therefore, such shocks can be responsible for the observed fluxes of He II  $\lambda 4686$  and other high ionization emission lines. The existence of these fast motions is supported by the presence of broad components, with velocities of hundreds km s<sup>-1</sup> (e.g., Izotov et al. 1996; Westmoquette et al. 2007), in the line profiles of the strongest emission lines in some H II/BCD galaxies and GH IIRs. We checked for the presence of broad components in the H $\alpha$  line profile of our sample galaxies. In Tol 0104-388 this emission line profile is symmetric and well represented by a single Gaussian, and does not show prominent low intensity broad components in the integrated spectrum. In the case of Tol 2146-291 the base of the H $\alpha$  (and other such as [OIII]  $\lambda 5007$ ) profile appears to be very broad, with a component similar to the ones observed in other BCD

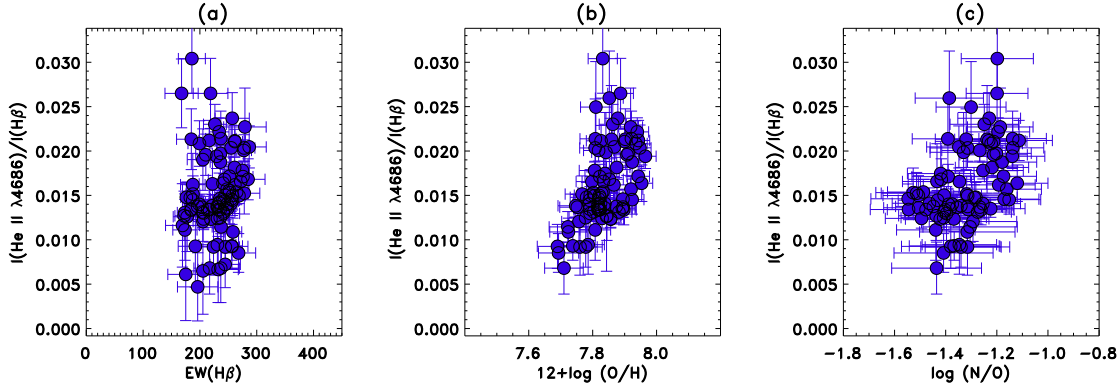


**Figure 15.** Intensity of the He II  $\lambda 4686$  emission line relative to  $H\beta$  as a function of the equivalent width of  $H\beta$ , oxygen abundance  $12 + \log(O/H)$  and  $\log(N/O)$  ratio for the galaxy Tol 2146-391.

galaxies (e.g., Izotov et al. 1996). Fig. 16 shows the spatial distribution of  $H\alpha$  emission line profiles in the  $0''.8 \times 0''.8$  spaxel size, as indicated in Sect. 4.1, for the galaxies Tol 0104-388 and Tol 2146-291, respectively. Again, we observe that the profile in the spaxels in Tol 0104-388 are well represented by a Gaussian, while in Tol 2146-291 we observe a broad base in the emission lines in the spaxels in the inner part of the map (see Fig. 16). In order to detect the presence of a broad component in these spaxels, we used the PAN<sup>3</sup> routine (Peak ANalysis) in IDL to fit two components to these profiles. Using this software, we found that these spaxels are well represented by a single Gaussian, with the exception of the spaxel on the peak of  $H\alpha$  emission. The broad component was estimated to be  $\sigma_{broad} < 100 \text{ km s}^{-1}$  with  $F(H\alpha)_{broad}/F(H\alpha)_{total} \sim 30\%$  and  $F(H\alpha)_{total} = F(H\alpha)_{narrow} + F(H\alpha)_{broad}$ .

Some evidences of the presence of two components in the emission line profile in this region are found in Bordalo & Telles (2011), where they observed a double component in the base of the emission lines  $H\alpha$ ,  $H\beta$ ,  $[O III]\lambda 4959$  and  $[O III]\lambda 5007$  in the integrated spectrum of Tol 2146-391. We must be careful in the interpretation of our kinematic results given that we use a medium resolution and not a high resolution grating. In any case, we may speculate that a broad component, eventually, could be properly resolved using high resolution spectroscopy in Tol 2146-391 and it may be associated with unresolved wind-driven shells (e.g., Chu & Kennicutt 1994). This scenario is plausible given that expanding structures have been detected in some compact H II/BCD galaxies, using  $H\alpha$  and/or  $H\beta$  emission line maps (e.g., Papaderos et al. 2002; Lagos et al. 2007). We have found in previous studies (Lagos et al. 2007) these filamentary structures in galaxies with one and multiple SF regions, such as Tol 0957-278, Tol 1004-296, UM 456, UM 462, UM 463, UM 483, IIZw 70 and Tol 1924-416. One for instance can note the filamentary structures generally very close to the star cluster complexes, to distances that range from  $\sim 100$  pc to  $\sim 1000$  pc, while the  $EW(H\beta)$  map of these galaxies shows these structures associated with large  $EW(H\beta)$  values (Lagos et al. 2007).

Finally, as we mentioned previously in this work, only

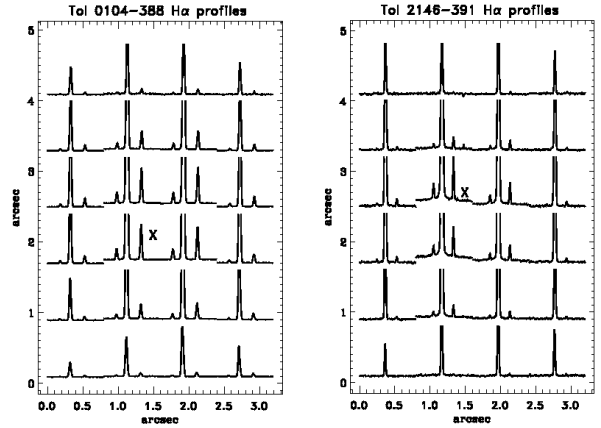


**Figure 16.** Spatial distribution of  $H\alpha$  profiles in the galaxies Tol 0104-388 and Tol 2146-291.

Tol 2146-391 was reported in the literature as a WR galaxy by previous studies (e.g., Masegosa et al. 1991). The examination over each individual  $0''.2$  spaxel and in the binned maps (see Fig. 14) and also in the integrated spectra (see Fig. 2), in both galaxies in our sample, do not reveal any clear stellar WR features. Given the spatial distribution of the nebular He II  $\lambda 4686$  emission in our two analyzed galaxies, this high ionizing radiation is likely associated with a mix of sources, where WR stars, HMXB and O stars cannot be excluded. Expanding shells powered by these unresolved star cluster/complexes (Lagos et al. 2011) can likely also be added as a source of ionizing radiation, at least in the case of Tol 2146-391.

### 4.3 Spatial and radial correlation of properties in the ISM

In Fig. 17 we show the  $\log(N/O)$  versus  $EW(H\beta)$  and  $12 + \log(O/H)$  vs.  $\log(N/O)$  for all  $0''.2$  spaxels in our two galaxies. In this fig., triangles correspond to the data points of Tol 0104-388 and circles correspond to the data points of Tol 2146-391. Izotov et al. (2006b) suggest that there is a dependence between the  $N/O$  ratio and the  $EW(H\beta)$ , for the entire galaxies, in the sense that the  $N/O$  ratio should increase with decreasing  $EW(H\beta)$ . Their

<sup>3</sup> <http://www.ncnr.nist.gov/staff/dimeo/panweb/pan.html>

conclusion is based on integrated spectra of a large sample of emission line galaxies with  $EW(H\beta)$  ranging from  $\sim 20$  to  $\sim 350$  Å. This trend was also observed recently by Brinchmann et al. (2008) and López-Sánchez & Esteban (2010a). But, no correlation between  $N/O$  and  $EW(H\beta)$  is found by Buckalew et al. (2005) using a smaller sample of galaxies. Izotov et al. (2006b) argue that the observed trend of  $N/O$  increasing as  $EW(H\beta)$  decreases is naturally explained by the expected ejection from WR stars. We observed in the upper panel of Fig. 17 that the  $EW(H\beta)$  values are rather constant, with a very small range of equivalent widths  $\Delta EW(H\beta) \sim 100$  Å, when the  $N/O$  ratio increases. Therefore, no correlation between  $EW(H\beta)$  and  $N/O$  is found in our sample galaxies. The reader must bear in mind that, in our case, we are concerned with the distribution of the physical properties within an individual galaxy and how that may affect the internal physical processes, as opposed to the statistical trends among different galaxies. If we compare the  $\log(N/O)$  vs.  $12+\log(O/H)$ , in the lower panel of Fig. 17 for Tol 2146-391, we see that the  $\log(N/O)$  values increase with the  $12+\log(O/H)$  abundance from  $\sim 7.70$  to  $\sim 7.97$ . This data point distribution has similar patterns to those found in BCD/HII galaxies (e.g., Izotov & Thuan 1999) of increasing  $N/O$  ratios with respect to the oxygen abundance. These studies suggest that at low metallicity ( $12+\log(O/H) < 7.6$ ) the N is associated with primary processes, at intermediate metallicities with a combination of primary and secondary processes, while at higher metallicities ( $12+\log(O/H) \gtrsim 8.30$ ) only with secondary processes. The inner region of Tol 2146-391 (near the peak of  $H\alpha$ ) present  $N/O$  ratios which are larger than those expected by the pure primary nature of nitrogen. This might be a signature of time delay between the release of oxygen and nitrogen (Kobulnicky & Skillman 1998), or even the presence of dynamical processes such as gas infall or outflow. In any case, for the metallicity of Tol 2146-391 secondary processes are unfeasible. No correlation is found between  $\log(N/O)$  vs.  $12+\log(O/H)$  in Tol 0104-388.

In Fig. 18 we show the radial distribution of oxygen abundance, nitrogen abundance,  $\log(N/O)$ ,  $EW(H\beta)$  with respect to the  $H\alpha$  continuum peak and  $EW(H\beta)$  with respect to  $12+\log(O/H)$  and  $12+\log(N/H)$  for the galaxy Tol 2146-391. The integrated properties of the galaxy are indicated with a continuous line and the two dotted lines show the uncertainties of these values at the  $1\sigma$  level. Statistically, the bulk of data points lie in a region of  $\pm 1\sigma$  around the integrated value of oxygen and  $\log(N/O)$  radial distribution. These results indicate that there is no significant variation across the galaxy. However, the  $12+\log(N/H)$  radial distribution shows that the highest values are located near the peak of continuum emission, with values reducing with radius.

If real, the observed trend of increasing  $12+\log(N/H)$  abundance in Tol 2146-391 would argue in favour of self-enrichment by the fresh heavy elements during the present burst of SF, on scales of hundreds of pc, or alternatively these heavy elements were produced during the previous burst of SF and dispersed in large scales across the galaxy in the current burst. If we assume that an instantaneous burst is a better description of the current burst in Tol 2146-391, we can obtain, using STARBURST99, that the mechanical luminosity released into the ISM via radiative winds and

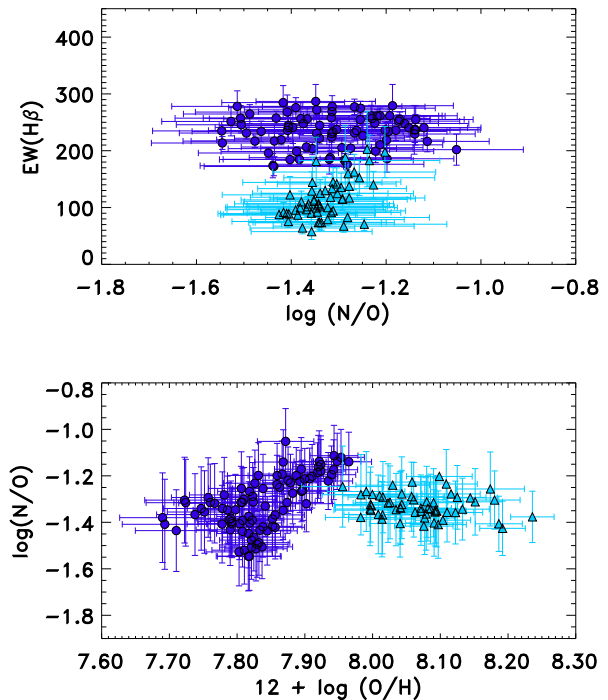


**Figure 17.**  $\log(N/O)$  ratio versus  $EW(H\beta)$  and  $12 + \log(O/H)$  ratio versus  $\log(N/O)$ . Triangles correspond to the data points of Tol 0104-388 and circles corresponds with the data points of Tol 2146-391.

SNe in order to produce a super-shell is  $\sim 12 \times 10^{39}$  erg  $s^{-1}$ . The radius in pc of an expanding super-shell can be written as  $R_s = 269(L_{38}/n_0)^{1/5} t_7^{3/5}$  (McCray & Kafatos 1987), where  $L_{38}$  denotes the mechanical luminosity in units of  $L_{38}$  erg  $s^{-1}$ ,  $t_7 = t/10^7$  yr and  $n_0$  is the density of the ambient gas in  $cm^{-3}$ . So, the distance reached by the super-shell at 4 Myr is  $R_s \sim 0.6$  kpc with a velocity of  $v_s \sim 241$  km  $s^{-1}$ , assuming  $n_0 \sim 100$   $cm^{-3}$ . Hence, the expansion of these shells is sufficient for producing, within the age of the current burst, the dispersion of the metal at a distance  $R_s \lesssim 0.4$  kpc. On the other hand, Peimbert et al. (2012) determined the physical conditions in Tol 2146-391 considering the presence of thermal inhomogeneities ( $t^2$ ). The high value of  $t^2$  found by Peimbert et al., in Tol 2146-391, agree with the idea that radiative shocks coming from SNe explosions have higher effect on the thermal structure of the galaxy. In any case, a conclusive assessment of this issue is not possible with the present data, but this scenario appears to be viable and agrees within the overall observed properties of Tol 2146-391.

As we mentioned previously in Sect. 4.2, the examination of each individual  $0''.2$  spaxel and in the binned maps (see Fig. 14), in both galaxies in our sample, does not reveal any clear WR feature. The detection of WR stars is not easy and different studies show different results. For example in the galaxy UM 420 López-Sánchez & Esteban (2010b), using long slit spectroscopy, detected the presence of WR stars, but using VLT-VIMOS observations James et al. (2010) did not find any evidence of WR signature in this galaxy. This discrepancy indicates that the detection of WR features in

galaxies depends on the quality of the spectra, location and size of the apertures (Schaerer et al. 1999). Therefore, if the detection of WR stars in Tol 2146-391 is not proven, the observed trend could be due to the outflow of previously enriched gas. Since the metallicity and composition of the ISM evolves with time, the super-shell wind will produce a metallicity gradient, with the inner parts containing a larger proportion of metals. In the case of Tol 2146-391, the presence of these energetic winds are supported by the observation of an irregular and broad component in the base of the emission lines (Bordalo & Telles 2011).

In any case, the results obtained in this work suggest that even though a slight gradient, in scales of hundreds of pc, of N is observed in the ISM of Tol 2146-391 (as result of the starburst activity) the properties across the galaxies are fairly well mixed. This suggests that the O and N enrichment and dispersion is likely related with a global process in the galaxies. Pérez-Montero et al. (2011) studied a sample of three BCD galaxies with high value of N. They found that the globally high N/O ratio in these objects is not likely produced by stellar winds coming from WR stars, but on the contrary, could be related more to other global processes affecting the metal content of the whole galaxy. We suggest that global hydro-dynamical effects, such as starburst-driven super-shells might be attributed to efficient transport and mixing of metals across the galaxies, so keeping the N/O ratio constant through the ISM at large scales. These no significant variation in abundance across the ISM of the galaxies would be indicative of uniform SF history, that is likely the case of low luminosity and compact H II galaxies, where the SF appear to be simultaneous over short timescales (Lagos et al. 2011). This scenario agrees with the idea that most of the He II  $\lambda 4686$  emission is produced by radiative shocks powered by a plethora of unresolved star clusters. Therefore, these H II galaxies are a genuine example of the simplest starburst occurring in galactic scale, possibly mimicking the properties one expects for young galaxies and/or H II galaxies at intermediate and high redshift.

## 5 CONCLUSIONS

Using new GMOS-IFU spectroscopic observations of the compact H II/BCD galaxies Tol 0104-388 and Tol 2146-391, we studied the spatial distribution of the high-ionization emission line He II  $\lambda 4686$  and the chemical pattern through the ISM of the galaxies in an extended region of  $3''.2 \times 5''$ , equivalent to  $\sim 1372 \text{ pc} \times 2058 \text{ pc}$  and  $\sim 1820 \text{ pc} \times 2730 \text{ pc}$  for Tol 0104-388 and Tol 2146-391, respectively. Based on the analysis of its properties, we have obtained the following results:

(i) The examination over each individual  $0''.2$  spaxel and also in the integrated spectra, in both galaxies in our sample, do not reveal any clear stellar WR features.

(ii) Both galaxies show the presence of the emission line He II  $\lambda 4686$  with an integrated intensity relative to  $H\beta$  of  $I(\text{He II } \lambda 4686)/I(H\beta) < 0.02$ . We did not detect a clear correlation between the spatial distribution of  $EW(H\beta)$ ,  $12 + \log(O/H)$  and  $\log(N/O)$  with respect to the hardness of this high-ionization radiation across the spaxels in Tol 2146-391.

(iii) Given the spatial distribution of He II  $\lambda 4686$  emission in our two analyzed galaxies, this high ionizing radiation is

likely associated with a mix of sources, where WR stars, HMXB and O stars cannot be excluded. While, expanding shells powered by a plethora of unresolved star clusters are likely producing most of the observed He II  $\lambda 4686$  emission in our sample galaxies, at least in Tol 2146-391.

(iv) We found some evidence that the  $12 + \log(N/H)$  radial distribution, in Tol 2146-391, shows a slight trend, with the values decreasing with distance from H $\alpha$  continuum peak. If real, this observed trend of  $12 + \log(N/H)$  abundance would argue in favour that these heavy elements were produced during the previous burst of SF and are currently dispersed by the expansion in the ISM of starburst-driven super-shells. However, the spatial constancy of the N/O ratio might be attributed to efficient transport and mixing of metals by hydro-dynamical effects during the previous episodes of SF.

All results presented here are suggestive that the physical conditions in these two galaxies, as in the case of the low luminosity and compact galaxy UM 408 (Lagos et al. 2009), vary in a very small dynamical range and are quite homogeneous. Therefore, the lack of significant variation in abundance across the ISM of the galaxies would be indicative of uniform SF history occurring in galactic scales.

## ACKNOWLEDGMENTS

We would like thank the anonymous referee for his/her comments and suggestions which substantially improved the paper. P.L. is supported by a Post-Doctoral grant SFRH/BPD/72308/2010, funded by FCT (Portugal). P.L. would like thank to Polychronis Papaderos and Andrew Humphrey for their very useful comments, suggestions and discussions which have improved the paper. Based on observations obtained at the Gemini Observatory, which is operated by the Association of Universities for Research in Astronomy, Inc., under a cooperative agreement with the NSF on behalf of the Gemini partnership: the National Science Foundation (United States), the Science and Technology Facilities Council (United Kingdom), the National Research Council (Canada), CONICYT (Chile), the Australian Research Council (Australia), Ministério da Ciência e Tecnologia (Brazil) and Ministerio de Ciencia, Tecnología e Innovación Productiva (Argentina). Gemini Program ID: GS-2004B-Q-59 and GS-2005B-Q-19.

## REFERENCES

- Abel T., Bryan G. L., & Norman M. L. 2002, *Sci*, 295, 93
- Allington-Smith J., Graham M., Content R., Dodsworth G., Davies R., Miller B. W., Jørgensen I., Hook I., Cramp-ton D., & Murowinski R. 2002, *PASP*, 114, 892
- Alloin D., Collin-Souffrin S., Joly M., & Vigroux J. M., 1979, *A&A*, 78, 200
- Baldwin J. A., Phillips M. M., & Terlevich R. 1981, *PASP*, 93, 5
- Bordalo V. & Telles E. 2011, *ApJ*, 735, 52
- Brinchmann J., Kunth D., & Durret F. 2008, *A&A*, 485, 657
- Buckalew B. A., Kobulnicky H. A., & Dufour R. J. 2005, *ApJS*, 157, 30

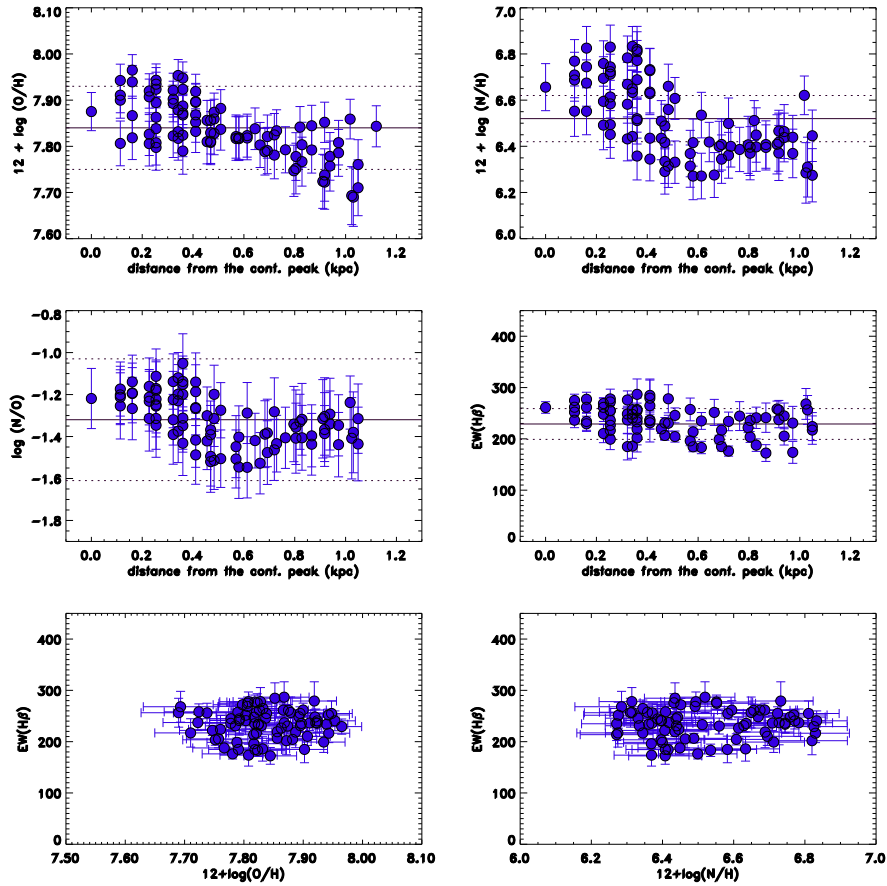


**Figure 18.**  $12 + \log(O/H)$ ,  $12 + \log(N/H)$ ,  $\log(N/O)$  ratio and  $EW(H\beta)$  as a function of the distance from the  $H\alpha$  continuum peak and  $12 + \log(O/H)$ ; and  $12 + \log(N/H)$  versus  $EW(H\beta)$  for the galaxy Tol 2146-391. The integrated properties are indicated with a black continuous line. The two dotted lines shows the uncertainties of these values.

Cairós, L. M., Caon, N., Papaderos, P., Noeske, K., Vílchez, J., M., Lorenzo, B. G., & Muñoz-Tuñón, C. 2003, *ApJ*, 593, 312

Cairós L. M., Caon N., Papaderos P., Kehrig C., Weilbacher P., Roth M., & Zurita C. 2009a, *ApJ*, 707, 1676

Cairós L. M., Caon N., Zurita C., Kehrig C., Weilbacher P., & Roth M. 2009b, *A&A*, 507, 1291

Cairós, L. M., Caon, N., Zurita, C., Kehrig, C., Roth, M., & Weilbacher, P. 2010, *A&A*, 520, 90

Cardelli, J. A., Clayton, G. C., & Mathis, J. S. 1989, *ApJ*, 345, 245

Campbell A., Terlevich R., & Melnick J. 1986, *MNRAS*, 223, 811

Chu Y.-H., & Kennicutt R. C. Jr. 1994, *ApJ*, 425, 720

de Mello D. F., Schaerer D., Heldmann J., & Leitherer C. 1998, *ApJ*, 507, 199

De Robertis M. M., Dufour R. J., & Hunt R. W. 1987, *JRASC*, 81, 195

Dopita M. A., & Sutherland R. S. 1996, *ApJS*, 102, 161

Dottori H. A. 1981, *Ap&SS*, 80, 267

Edmunds M. G. & Pagel B. E. J. 1978, *MNRAS*, 185, 77

Fricke K. J., Izotov Y. I., Papaderos P., Guseva N. G., & Thuan T. X. 2001, *AJ*, 121, 169

Garnett D.R., 1990, *ApJ* 363, 142

Garnett D. R. 1992, *AJ*, 103, 1330

Garnett D. R., Kennicutt R. C. Jr., Chu Y.-H., & Skillman E. D. 1991, *ApJ*, 373, 458

Guseva N. G., Izotov Y. I., & Thuan T. X. 2000, *ApJ*, 531, 776

Guseva N. G., Izotov Y. I., Papaderos P., & Fricke K. J. 2007 *A&A*, 464, 885

Guseva N. G., Izotov Y. I., Stasińska G., Fricke K. J., Henkel C., & Papaderos P. 2011, *A&A*, 529, 149

Guseva, N. G.; Izotov, Y. I.; Fricke, K. J.; Henkel, C. 2012, arXiv:1203.5268v1

Hodge P. W. 1974, *ApJ*, 191, 21

Hook I., Jørgensen I., Allington-Smith J. R., Davies R. L., Metcalfe N., Murowinski R. G., & Crampton D. 2004, *PASP*, 116, 425

Izotov, Y. I., Dyak, A. B., Chaffee, F. H., Foltz, C. B., Kniazev, A. Y., & Lipovetsky, V. A. 1996, *ApJ*, 458, 524

Izotov Y. I., & Thuan T. X. 1999, *ApJ*, 511, 639

Izotov Y. I., Chaffee F. H., & Schaerer D. 2001, *A&A*, 378, 45

Izotov Y. I., Papaderos P., Guseva N. G., Fricke K. J., & Thuan T. X. 2004, *A&A*, 421, 539

Izotov Y. I., Schaerer D., Blecha A., Royer F. & Guseva N. G., North, P 2006a, *A&A*, 459, 71

Izotov Y. I., Stasińska G., Meynet G., Guseva N. G., & Thuan T. X. 2006b, *A&A*, 448, 955

- James B. L., Tsamis Y. G., & Barlow M. J. 2010, MNRAS, 401, 759
- Kewley L. J., Dopita M. A., Sutherland R. S., Heisler C. A., Trevena J. 2001, ApJ, 556, 121
- Kehrig C., Vílchez J. M., Telles E., Cuisinier F., Pérez-Montero E. 2006, A&A, 457, 477
- Kingsburgh, R. L. & Barlow, M. J. 1994, MNRAS, 271, 257
- Kobulnicky H. A., Skillman E. D., Roy J.-R., Walsh J. R., & Rosa M. R. 1997, ApJ, 477, 679
- Kobulnicky H. A., & Skillman E. D. 1998, ApJ, 497, 601
- Kunth D., & Sargent W. L. W. 1983, ApJ, 273, 81
- Lagos P., Telles E., & Melnick J. 2007, A&A, 476, 89
- Lagos P., Telles E., Muñoz-Tuñón C., Carrasco E. R., Cuisinier F., & Tenorio-Tagle G. 2009, AJ, 137, 5068
- Lagos P., Telles E., Nigoche-Netro A., & Carrasco E. R. 2011, AJ, 142, 162
- Leitherer C., et al. 1999, ApJS, 123, 3
- López-Sánchez A. R., & Esteban C. 2010a, A&A, 517, 85
- López-Sánchez A. R., & Esteban C. 2010b, A&A, 516, 104
- McCray R., & Kafatos M. 1987, ApJ, 317, 190
- Masegosa J., Moles M. & del Olmo A. 1991, A&A, 244, 273
- Martin C. L. 1998, ApJ, 506, 222
- Meynet G., & Maeder A. 2005, A&A, 429, 581
- Monreal-Ibero A., Vílchez J. M., Walsh J. R., & Muñoz-Tuñón C. 2010, A&A, 517, 27
- Osterbrock D. E., & Ferland G. J. 2006, Astrophysics of gaseous nebulae and active galactic nuclei, 2nd. edn. (Sausalito, CA: University Science Books)
- Papaderos, P., Loose, H. H., Thuan, T. X., & Fricke, K. J. 1996, A&AS, 120, 207
- Papaderos, P., Izotov, Y. I., Thuan, T. X., Noeske, K. G., Fricke, K. J., Guseva, N. G., & Green, R. F. 2002, A&A, 393, 461
- Papaderos P., Guseva N. G., Izotov Y. I., Noeske K. G., Thuan T. X., & Fricke K. J. 2006, A&A, 457, 45
- Pagel B. E. J., Simonson E. A., Terlevich R. J., & Edmunds, M. G. 1992, MNRAS, 255, 325
- Peimbert, A., Peña-Guerrero, M. A., & Peimbert, M. 2012, arXiv:1204.4507v1
- Peña M., Ruiz M. T., & Maza, J. 1991, A&A, 251, 417
- Pérez-Montero E., Vílchez J. M., Cedrés B., Hägele G. F., Mollá M., Kehrig C., Díaz A. I., García-Benito R., & Martín-Gordón D. 2011, A&A, 532, 141
- Sargent, W. L. W., & Searle, L. 1970, ApJ, 162, 155
- Stasińska G. 1990, A&AS, 83, 501
- Schaerer D. 1996, ApJ, 467, 17
- Schaerer D., & de Koter A. 1997, A&A, 322, 598
- Schaerer D., Contini T., & Pindao M. 1999, ApJ, 497, 618
- Schaerer D. 2002, A&A, 382, 28
- Schaerer D. 2003, A&A, 397, 527
- Telles, E., & Terlevich R. 1997, MNRAS, 286, 183
- Telles E., Melnick J., & Terlevich R. 1997, MNRAS, 288, 78
- Thuan T. X., Bauer F. E., Papaderos P., & Izotov Y. I. 2004, ApJ, 606, 213
- Thuan T. X., & Izotov Y. I. 2005, ApJS, 161, 240
- van Zee, L., Salzer, J. J., & Haynes, M. P. 1998, ApJ, 497, 1
- Westmoquette M. S., Exter K. M., Smith L. J., & Gallagher J. S. 2007, MNRAS, 381, 894